Efficient electronic structure calculations for extended systems of coupled quantum dots using a linear combination of quantum dot orbitals method

Alexander Mittelstädt,* Ludwig A. Th. Greif, Stefan T. Jagsch, and Andrei Schliwa
Institut für Festkörperphysik, Technische Universität Berlin, Hardenbergstr. 36, 10623 Berlin, Germany

(Received 28 November 2019; revised 8 February 2021; accepted 9 February 2021; published 1 March 2021)

We present a novel "linear combination of atomic orbitals"-type of approximation, enabling accurate electronic structure calculations for systems of up to 20 or more electronically coupled quantum dots. Using realistic single quantum dot wave functions as a basis to expand the eigenstates of the heterostructure, our method shows excellent agreement with full 8-band $\boldsymbol{k}\cdot\boldsymbol{p}$ calculations, exemplarily chosen for our benchmarking comparison, with orders of magnitude reduction in computational time. We show that, to correctly predict the electronic properties of such stacks of coupled quantum dots, it is necessary to consider the strain distribution in the whole heterostructure. Edge effects determine the electronic structure for stacks of $\lesssim$10 quantum dots, after which a homogeneous confinement region develops in the center. The overarching goal of our investigations is to design a stack of vertically coupled quantum dots with an intraband staircase potential suitable as an active material for a quantum-dot-based quantum cascade laser. Following a parameter study in the $In_xGa_{1-x}As/GaAs$ material system, varying quantum dot size, material composition, and interdot coupling strength, we show that an intraband staircase potential of identical transitions can, in principle, be realized. A species library we generated for over 800 unique quantum dots provides easy access to the basis functions required for different realizations of heterostructures. In the associated paper [Mittelstädt *et al.*, Phys. Rev. B **103**, 115301 (2021)], we investigate room temperature lasing of a terahertz quantum cascade laser based on a two-quantum-dot unit cell superlattice.

DOI: 10.1103/PhysRevB.103.115302

I. INTRODUCTION

The unique electronic properties of stacked quantum dots (QDs) offer enhancements not only for optical semiconductor devices such as lasers, optical amplifiers, and single-photon devices, but can also be advantageous for quantum cascade lasers (QCLs). In QCLs, amplification of radiation is realized via intraband transitions of electrons running down a staircase potential generated by a semiconductor superlattice at an external bias. As proposed in Refs. [1–4], QD-based QCLs can benefit from intrinsically reduced electron-phonon scattering processes, free-carrier absorption processes, and an intrinsically narrow gain spectrum of electronically coupled QDs, resulting in improved temperature resilience and greatly reduced laser threshold current densities. The advantages of a three-dimensional confinement of carriers in QCLs are demonstrated by several theoretical studies and experiments on quantum cascade structures utilizing QDs [2,5–7], but also using quantum well-based structures in strong magnetic fields splitting the 2D subbands into a series of Landau levels [8–11].

A realization of a QCL based on a superlattice solely build of coupled QDs, cf. Fig. 1, however, is still lacking mainly for two reasons. On the one hand, a precise control over the desired structure during epitaxy, i.e., over the QD's size, shape, composition, and their relative vertical position to each other, is needed. On the other hand, to arrive at a promising device design proposal, a rigorous simulation of the electronic structure of stacks of QDs requires plenty of iterations already at the modeling stage. The effort to find suitable design parameters scales with the computational cost for an iteration of simulating the electronic structure of a

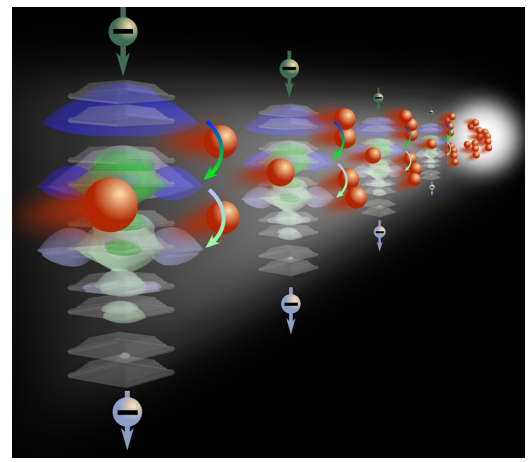

FIG. 1. Schematic illustration of light amplification in a QD cascade structure driven via an external bias. Stacks of electronically coupled QDs build a staircase potential providing optical transitions (blue electron densities) and states making nonradiative relaxation of carriers efficient (green electron densities).

*mittelstaedt@tu-berlin.de

realistic system of more than ten coupled QDs, as well as calculating dozens of electronic states. However, regarding the theoretical proposals and calculations of QD-based QCLs, the literature is based solely on assumptions of the electronic structure of such extended systems. Most investigations on the electronic properties of coupled QDs within the framework of tight-binding and 8-band $\boldsymbol{k}\cdot\boldsymbol{p}$-models [12–16] involve just a stack of two QDs and a few involve nine layers of QDs calculating a maximum of 12 electronic states, where, in particular, the tight-binding models are limited by large systems containing tens of millions of atoms.

In this paper, we demonstrate a novel "linear combination of atomic orbitals"-type of approximation, making simulations of electronic properties of large systems of 20 and more electronically coupled QDs very efficient. Our "linear combination of quantum dot orbitals" method (LCQO) works the following way. First, a library of QDs, systematically covering different sizes, shapes, and chemical composition profiles, together with the associated single-particle eigenstates, is created. Then, driven by the desired target properties, systems of coupled QDs are virtually assembled together with the associated Hamiltonian, which is then expanded using the library of single-QD wave functions as a basis. The method as implemented herein uses basis functions calculated via an 8-band $\boldsymbol{k}\cdot\boldsymbol{p}$ model including a realistic structure, strain, and strain-induced internal fields, but can be implemented as such on any atomistic or continuum model. The resulting LCQO eigenstates show an excellent agreement in a side-by-side comparison with a full 8-band $\boldsymbol{k}\cdot\boldsymbol{p}$ simulation for stacks of two QDs and a benchmark comparison of the two methods for an exemplarily chosen system of ten stacked QDs shows a reduction of at least three orders of magnitude in computational time. By using the LCQO approach, we are able to take into account the individual three-dimensional morphology of each QD within the stack, calculate strain, and strain-induced internal fields of the whole structure as well as interdot electronic coupling.

We show why simulating ten or more QDs is necessary to obtain uniform conduction band energy splittings and electron probability densities along the QD chain, highlighting the influence of strain and piezoelectric fields on the band structure of electronically coupled QDs. A simulation of 20 QDs is, therefore, necessary to get an intraband staircase potential of several identical transitions as adaptable for a QD cascade active region design.

This paper is organized as follows. After introducing the method of calculation and a comparison to an 8-band $\boldsymbol{k}\cdot\boldsymbol{p}$ simulation, we analyze the electronic properties of stacks of $In_xGa_{1-x}As$ QDs embedded in a GaAs matrix with a focus on conduction band intraband transitions as applicable in QCLs based on a QD superlattice and demonstrate the necessity of simulating the entire heterostructure. Subsequently, we provide a parameter study by varying quantum dot size, material composition, and interdot coupling strength of stacks of QDs. The last part shows that a uniform staircase potential of identical transitions of an exemplary QD heterostructure can be realized and highlights the impact of applying an external bias. In the associated paper Ref. [17], we study a QCL with QD chains as gain material, suitable for light amplification in the THz regime and device operation up to room temperature. The underlying parameter studies were feasible thanks to the orders of magnitude reduction in computation time and access to the pre-built QD species library.

II. LINEAR COMBINATION OF QUANTUM DOT ORBITALS METHOD

Along the lines of a linear combination of atomic orbitals (LCAO) method, a large system M of coupled QDs is split into subsystems I of single QDs, so that

$$M := \bigcup \{I \mid I \text{ is a single QD subsystem}\}, \tag{1}$$

for which sets of single-particle states $\{|\varphi_1^I\rangle, \ldots, |\varphi_n^I\rangle\}$ can be efficiently calculated. As illustrated in Figs. 2(a) and 2(b), these single-particle wave functions are calculated for different QD species building a library of wave functions then used as a basis in the LCQO approximation of the eigenstates of the hybrid system

$$\left|\psi_i^{\mathrm{LCQO}}\right\rangle = \sum_{k=1}^{m} a_{ik} \left|\varphi_k^M\right\rangle , \tag{2}$$

where $\{|\varphi_k^M\rangle\} := \cup\{|\varphi_j^I\rangle\}$ and the $\{|\varphi_k^M\rangle\}$ are partially superimposed. In this way, the number of coefficients $\{a_1(\boldsymbol{r}), \ldots, a_m(\boldsymbol{r})\}$ in the variational problem of finding the eigenstates of M is reduced to $m = |M|\times n$, where $|M|$ is the number of coupled QDs and n is the number of single-particle states used as basis functions per QD. The number of coefficients m is therefore independent of the number of grid points of the $|\varphi_k^M\rangle$. We note that the amount of basis functions n for each QD is not necessarily a constant and could, for example, be the number of bound states for each QD in a system composed of QDs differing in size or material composition. When creating the basis for the LCQO method, the goal is to approximate the eigenstates of the heterostructure as best as possible with a limited set of basis functions, which is achieved by using realistic single QD wave functions. To find the eigenstates of M, we adopt the Rayleigh-Ritz variational principle for the energy functional [18]. Using the expansion in Eq. (2),

$$\varepsilon_i\left[\psi_i^{\mathrm{LCQO}}\right] = \frac{\left\langle\psi_i^{\mathrm{LCQO}}\middle|\boldsymbol{H}\middle|\psi_i^{\mathrm{LCQO}}\right\rangle}{\left\langle\psi_i^{\mathrm{LCQO}}\middle|\psi_i^{\mathrm{LCQO}}\right\rangle} \tag{3}$$

$$= \sum_{k,l=1}^{m} \frac{a_{il}^* a_{ik} \overbrace{\left\langle\varphi_l^M\middle|\boldsymbol{H}\middle|\varphi_k^M\right\rangle}^{H_{lk}}}{a_{il}^* a_{ik} \underbrace{\left\langle\varphi_l^M\middle|\varphi_k^M\right\rangle}_{S_{lk}}} \tag{4}$$

where $\boldsymbol{H}$ denotes the hybrid system's Hamiltonian. Notably, the system Hamiltonian $\boldsymbol{H}$ contains not a mere superposition of the electrostatic potentials of the QD subsystems, which would be an oversimplification for systems of QDs, cf. Sec. III B, but instead considers the strain distribution in M. Since the strain state and the resulting piezoelectric fields in the QD heterostructure strongly depend on the actual QD configuration as well as geometry and material composition of the individual QDs, the Hamiltonian has to be generated

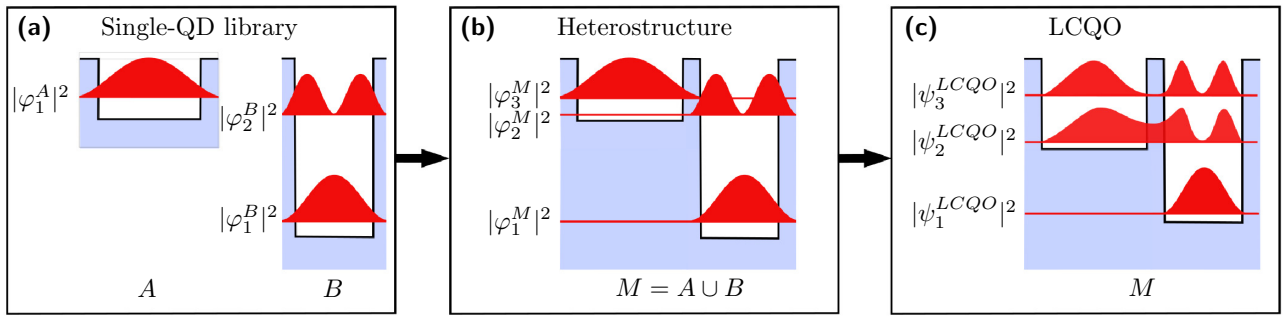

FIG. 2. Schematic illustration of the LCQO-method for a system of two QDs. (a) A library of basis functions for different QD species $(A, B, \ldots)$ is created. (b) The heterostructure is formed using the library's QDs as building blocks $(M = A \cup B)$, whereby the subsystems are partially superimposed. The system's Hamiltonian is generated, considering the strain distribution and resulting piezoelectric potentials in the in the hybrid system M. (c) The eigenstates of the heterostructure $|\psi_i^{\mathrm{LCQO}}\rangle$ are expanded in the union of the basis $\{|\varphi_k^M\rangle\} := \{|\varphi_j^A\rangle\} \cup \{|\varphi_l^B\rangle\}$.

individually for each unique assembly. Varying the energy functional in Eq. (4) with respect to the expansion coefficients $\delta\varepsilon_i/\delta a_{il}^*$, and minimizing the energy, leads to the generalized eigenvalue problem

$$\begin{pmatrix} H_{11} & \cdots & H_{1m} \\ \vdots & \ddots & \vdots \\ H_{m1} & \cdots & H_{mm} \end{pmatrix} \begin{pmatrix} a_1 \\ \vdots \\ a_m \end{pmatrix} = \varepsilon \begin{pmatrix} S_{11} & \cdots & S_{1m} \\ \vdots & \ddots & \vdots \\ S_{m1} & \cdots & S_{mm} \end{pmatrix} \begin{pmatrix} a_1 \\ \vdots \\ a_m \end{pmatrix} \tag{5}$$

that yields m eigenvalues ε_i and corresponding eigenvectors $|a_i\rangle$, containing the coefficients a_{ik} of the LCQO eigenfunctions $|\psi_i^{\mathrm{LCQO}}\rangle$, cf. Fig. 2(c).

So far, the LCQO method is universal and could be implemented on top of any atomistic or continuum model used to calculate the electronic states of the single QDs. In the present work, we exemplarily use an established 8-band $\boldsymbol{k}\cdot\boldsymbol{p}$ model, including strain-induced internal fields up to second-order piezoelectricity, to calculate the single-particle wave functions of the individual QDs, see Refs. [19–21] and the Supplemental Material in Ref. [22] for details; also see Refs. [23–37] and references therein. Within the 8-band $\boldsymbol{k}\cdot\boldsymbol{p}$ model, the LCQO basis is expanded according to

$$|\varphi_k^M\rangle = \sum_{o=1}^{8} b_{ko}\,|\xi_o\rangle\,, \tag{6}$$

with the complex-valued envelope-function coefficients b_{ko} and the atom-like Bloch functions $|\xi_o\rangle$. The LCQO eigenfunctions in Eq. (2) are then given as

$$|\psi_i^{\mathrm{LCQO}}\rangle = \sum_{k=1}^{m} a'_{ik} \sum_{o=1}^{8} b_{ko}\,|\xi_o\rangle\,. \tag{7}$$

A performance benchmarking of the LCQO method compared to a full 8-band $\boldsymbol{k}\cdot\boldsymbol{p}$ calculation for exemplary systems of two and ten QDs is provided in Fig. 3. The benchmark reveals already for the calculation of 20 single-particle states in a stack of ten QDs a reduction of at least three orders of magnitude in computational time for the LCQO method compared to a full 8-band $\boldsymbol{k}\cdot\boldsymbol{p}$ calculation. Since the calculation time for the $\boldsymbol{k}\cdot\boldsymbol{p}$ method increases strongly with the number of states, it is impractical to calculate more states, while with the LCQO method, 50 and more eigenstates can be calculated very effectively.

III. RESULTS

We investigate the electronic structure of vertically coupled $In_xGa_{1-x}As/GaAs$ QDs, with the goal to design a heterostructure with an intraband staircase potential suitable for a QD-QCL active region. A decisive advantage of the LCQO method is that a library of basis functions for realistic single QDs can be prepared to facilitate a parameter series of coupled QD systems, cf. Fig. 2. We created such a species library for over 800 $In_xGa_{1-x}As/GaAs$ QDs varying in size, vertical aspect ratio AR_v (height h divided by the base diameter d_b), and material composition, within experimentally realistic limits. In agreement with transmission electron microscopy (TEM) investigations in Refs. [38,39], the $In_xGa_{1-x}As$ QDs are modeled as truncated pyramids with a sidewall inclination of 40°, embedded in a GaAs matrix. With the exception of the parameter series in Sec. III C, results are presented for a model QD with a base diameter of 20.8 nm, and a height of 2.8 nm ($AR_v = 0.135$), along with experimental reports in Refs. [40–43]. In comparison to the literature, our model QD has a slightly smaller AR_v to account for material

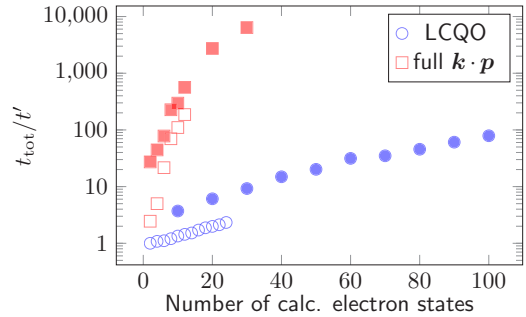

FIG. 3. A comparison of calculation time between the 8-band $\boldsymbol{k}\cdot\boldsymbol{p}$-simulations (red squares) and the LCQO method (blue circles). Empty and filled symbols denote a stack of two and ten QDs, respectively. The total calculation time t_{tot} is normalized to an LCQO simulation, calculating two states in a stack of two QDs. The simulations were performed on AMD Opteron 6274 processors, where the $\boldsymbol{k}\cdot\boldsymbol{p}$-simulations were parallelized using four threads.

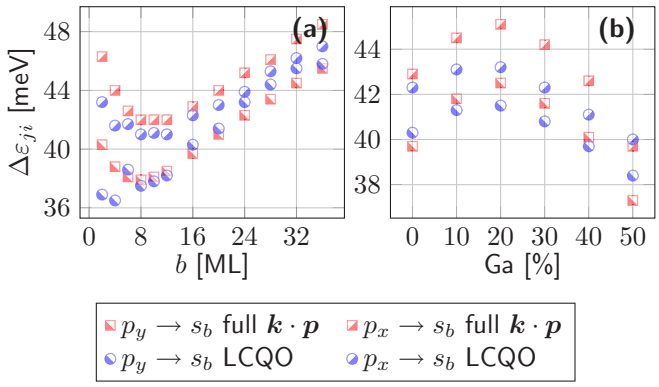

FIG. 4. Evolution of the energetic positions of the p-to-s transitions for a stack of two identical QDs as a function of (a) barrier width and (b) material composition for the $\boldsymbol{k}\cdot\boldsymbol{p}$ model (red squares) and the LCQO model (blue circles). Semifilled circles and squares distinguish the p_y and p_x-to-s transitions.

interdiffusion in real systems since experiments show QDs exhibiting a composition gradient with a decreasing indium content, which, in turn, results in a confinement region smaller than the QDs geometry. As basis functions per QD, we calculate the five lowest Kramers-degenerate electron states (ten states per QD), which is the number of bound electrons in the model QD. This base size results in an excellent agreement of the energy eigenvalues and envelopes, as shown below for the states in a stack of two QDs. In addition, the Supplemental Material [22] shows that already with a base of $n = 10$ the energy eigenvalues ε_i of the lowest four Kramers-degenerated orbitals converge against the values of the full $\boldsymbol{k}\cdot\boldsymbol{p}$ calculation within a 0.1% error. To solve the eigenvalue problem in Eq. (5), we use a standard linear algebra package (LAPACK) with a finite-difference grid resolution of two monolayers (MLs) of GaAs (5.6503 Å), equally in the case of the full $\boldsymbol{k}\cdot\boldsymbol{p}$ calculations.

A. Direct comparison between LCQO and a full 8-band $\boldsymbol{k}\cdot\boldsymbol{p}$ calculation

We compare the results of LCQO and full 8-band $\boldsymbol{k}\cdot\boldsymbol{p}$ calculations for stacks of two identical $In_xGa_{1-x}As$ QDs. Figure 4 shows the evolution of the two intraband transitions $|\psi_{p_{y,x}}\rangle \rightarrow |\psi_{s_b}\rangle$ in the system as a function of QD separation (coupling strength) and material composition for both methods. The eigenstates $|\psi_{p_{y,x}}\rangle$ and $|\psi_{s_b}\rangle$ have an odd (p-like) and even (s-like) symmetry [21], respectively, allowing optical transitions in agreement with parity selection rules. The LCQO method results and full 8-band $\boldsymbol{k}\cdot\boldsymbol{p}$ calculations are indicated by blue circles and red squares, respectively. In Fig. 4(a), the separating barrier width b is varied between 2 and 36 MLs in steps of 2 MLs, for two $In_{1.0}Ga_{0.0}As$ QDs, mapping the transition from strong to vanishing interdot coupling. Figure 4(b) shows the influence of an increasing gallium content up to 50% (in steps of 10%) on the transition energies at a constant barrier width of 16 MLs. The methods agree well in both series and produce similar transition energies with deviations $\lesssim$4 meV, smaller than the overall tuning range. The physical origin of the global minimum around $b = 10$ MLs in Fig. 4(a) will be discussed in detail in Sec. III C. Figure 5 shows the probability density $|\psi_i|^2$ for the first four Kramers-degenerate electron states for $b = 16$ MLs calculated using the full 8-band $\boldsymbol{k}\cdot\boldsymbol{p}$ (top) and LCQO method (bottom). Both probability density and symmetry of the eigenstates found using the LCQO method are in excellent agreement with the full 8-band $\boldsymbol{k}\cdot\boldsymbol{p}$ results. Overall, the LCQO method maps the electronic structure of coupled QDs excellently and provides realistic results comparable to a full $\boldsymbol{k}\cdot\boldsymbol{p}$ calculation.

B. Impact of hydrostatic strain and piezoelectricity on stacks of electronically coupled QDs

The lattice mismatch of 0.4 Å between InAs and GaAs results in a highly strained heterostructure. In a simplified picture, the electronic states of the coupled QDs shift linearly with the hydrostatic strain e_h [36]. Figure 6(a) depicts the hydrostatic strain distribution for three exemplary systems of $In_{1.0}Ga_{0.0}As$ QDs: a single QD and stacks of two and ten QDs, with a separating barrier width of $b = 8$ MLs. The larger lattice constant of InAs leads to a compressive strain within the single QD in Fig. 6(a). Subsequent stacking of QDs results in a cumulative compressive strain for the QDs in the center, while strain relaxation mainly occurs at the top and bottom of the stack. For the stack of ten QDs, the strain distribution is more or less uniform in the stack's central region, cf. shaded area in Fig. 6. This is also reflected in the distribution of the piezoelectric potential ϕ in Fig. 6(c). For a single QD, the piezoelectric potential vanishes inside

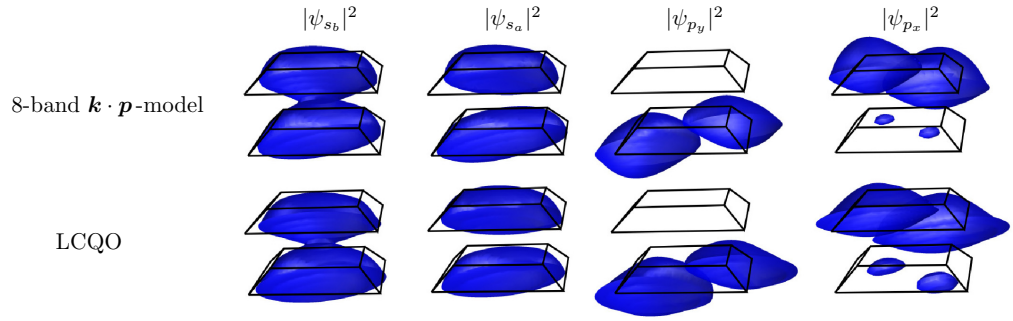

FIG. 5. Probability densities of the first four Kramers-degenerated electron states (isosurface at 90%) for the 8-band $\boldsymbol{k}\cdot\boldsymbol{p}$ model and the LCQO method, respectively. The system considered is a stack of two identical $In_{1.0}Ga_{0.0}As$ QDs with a barrier width of $b = 16$ MLs showing binding and antibinding s-type orbitals, $|\psi_{s_b}|^2$ and $|\psi_{s_a}|^2$, respectively, followed by p-type orbitals $|\psi_{p_y}|^2$ and $|\psi_{p_x}|^2$, respectively.

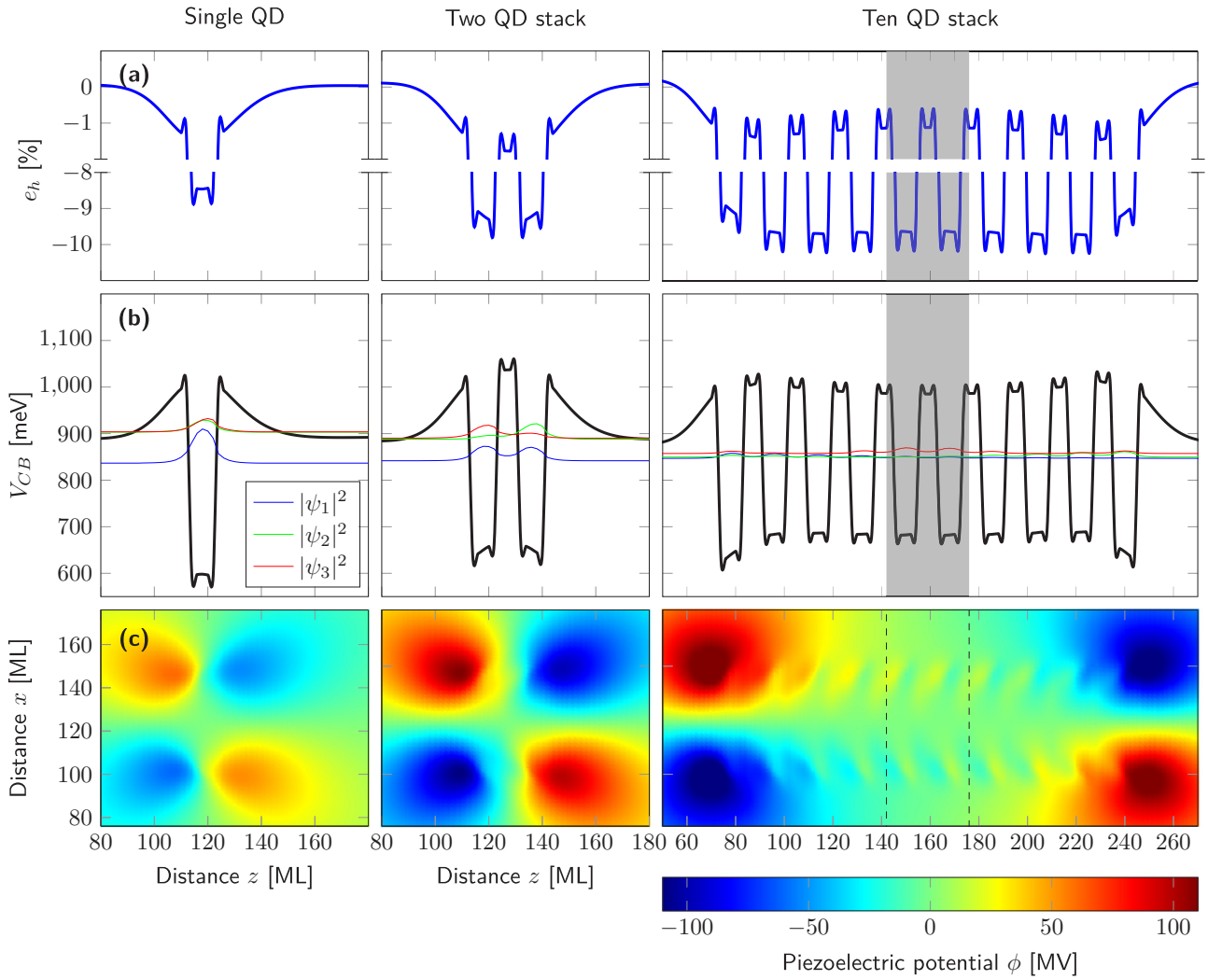

FIG. 6. Diagrams illustrating the hydrostatic strain, piezoelectricity, and the conduction band edge for a single QD and stacks of two and ten identical $In_{1.0}Ga_{0.0}As$ QDs. Here, the barrier width is set to $b = 8$ MLs and the wetting layer is omitted. (a) The distribution of the hydrostatic strain e_h and (b) the conduction band edge evolution V_{CB}. (c) The corresponding distribution of the piezoelectric potential within the (001)-plane trough the center of the QD stacks. The $|\psi_i(z)|^2$ show the probability densities of the first three Kramers-degenerate electron states.

the QD and shows a quadrupole-like distribution outside the QD, with inverted polarity at the top and bottom interfaces. As a result, the superimposed single QD potentials cancel each other out in the central region of the stack and are amplified at both ends of the chain, cf. Fig. 6(c). Fundamentally, the vanishing piezoelectric field inside the QDs and the symmetry of the quadrupole-like potential are linked to the first- and second-order piezoelectricity, as shown in Ref. [21]. Both the inhomogeneous strain distribution and the resulting piezoelectricity impact the electronic structure by shifting the conduction band edge V_{CB}, cf. solid black line in Fig. 6(b). In the uniform central region, we expect to find cascades of electron states, delocalized over neighboring QDs, suitable to generate the staircase potential required for a QCL active region. The probability densities $|\psi_i(z)|^2$ for the three lowest Kramers-degenerate electron states are shown in Fig. 6(b) exemplarily. As expected, the density of the first two states is localized within the QDs at the QD-chain edges, having the lowest V_{CB} potential. The third state's density (red) is already delocalized within the QD-chains central region and provides an s-type orbital constituting a "ground state" within a staircase-potential buildup at a certain applied external bias. The energetic sequence of the orbitals, as they occur in coupled QDs, depends decisively on the coupling strength and thus on the interdot distances. To illustrate this, we investigate the orbital symmetry of the lowest conduction band states in two coupled QDs as a function of the barrier width. Figure 7(a) shows the evolution of the energetic position ε_i of the lowest Kramers-degenerate electron states for the stack of two QDs discussed in Fig. 4(a). For strong QD coupling, cf. shaded area in Fig. 7(a), we find the conventional single-QD s_b-/p-/p-type orbital sequence, with the binding s-type orbital as the ground state, providing the two optically active intraband transitions investigated throughout this work. With the increasing separation of the QDs, the antibinding s-type orbital is lowered in energy, until for $b \gtrsim 12$ MLs, the orbital sequence is changed to s_b-/s_a-/p-/p-type. Above a specific separation ($b = 36$ MLs for the QDs considered), the

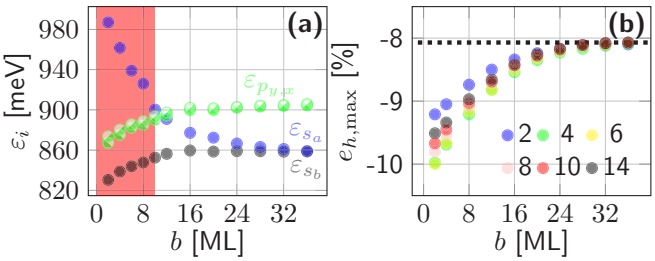

FIG. 7. Evolution of the state's absolute energy and hydrostatic strain. (a) Energetic position of Kramers-degenerate electronic states ε_i as a function of the separating barrier width b in a pair of two $In_{1.0}Ga_{0.0}As$ QDs. Filled and semifilled circles denote the binding s_b-, antibinding s_a-, and p-type orbitals (black, blue, and green), respectively. (b) Maximum negative hydrostatic strain $e_{h,\max}$ as a function of the barrier width b for an isolated pair of coupled QDs (blue) and the two central QDs in stacks of 4 to 14. The dotted line represents the hydrostatic strain within a single QD.

two s-type orbitals are no longer hybridized and each can be associated with one of the electronically uncoupled QDs. A remaining energy difference is due to different strain states and long-range piezoelectric fields in both QDs. Figure 7(b) compares the hydrostatic strain state of an isolated system of two coupled QDs with the two QDs in the center of stacks of 4 to 14 QDs. A clear difference is visible in the strong coupling regime. The hydrostatic strain shows a maximum for the two QDs in the central region of the stacks of four and six QDs and then decreases again with the number of QDs building the QD chain. This is due to the lattice being deformed irregularly at the edges of the QD chain, where the relaxation of the hydrostatic strain occurs. In all cases, the hydrostatic strain state of a single QD is recovered for separations $b > 36$ MLs.

C. Intraband transition energies as a function of QD size, material composition, and coupling strength

In this section, we explore the influence of interdot coupling strength, QD material composition, and QD size on the intraband transition energies for a stack of ten model QDs. Based on the knowledge from the preceding section, we investigate the electronic properties of the homogeneous central region of the QD stack that is eligible for a staircase potential with constant energy spacings. In this regard, ten is the minimum number of coupled QDs for the edge effects to be converged, leading to a flat conduction band edge and constant hydrostatic strain within the two central QDs, cf. shaded area in Fig. 6. In Fig. 8, the evolution of the p-to-s intraband transition energies in the central QD pair is shown as a function of separating barrier width b [Fig. 8(a)] and QD material composition [Fig. 8(b)], as well as QD size [Figs. 8(c) to 8(e)], where height, base diameter, and vertical aspect ratio are kept constant, respectively, for $b = 16$ MLs. For strongly coupled QDs, we observe a red-shift of the transition energies with increasing barrier width, up to a global minimum at $b \approx 8$ MLs, which coincides with the change in orbital sequence discussed above. With increasing gallium content, the transition energy shows a maximum at $In_{0.8}Ga_{0.2}As$ for the p_x-to-s and a monotonic decrease for the p_y-to-s transition. This is due to a V_{CB} conduction band potential in the QDs increasing

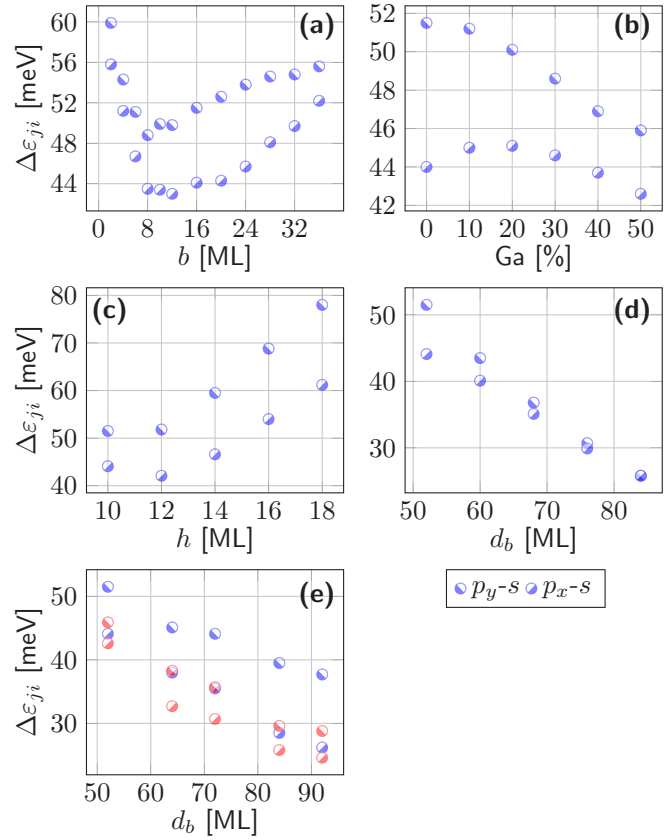

FIG. 8. Evolution of the transition energy $\Delta\varepsilon_{ji}$ of the p-to-s intraband transitions for the two central QDs in a stack of ten identical QDs as a function of (a) barrier width b, (b) QD material composition, and (c)–(e) size for a constant base diameter d_b, height h, and aspect ratio AR_v, respectively. Except for (b) and red symbols in (e), $In_{1.0}Ga_{0.0}As/GaAs$ QDs are considered and separated by $b = 16$ MLs. The red semifilled circles in (e) show the transition energies for $In_{0.5}Ga_{0.5}As/GaAs$ QDs at a constant aspect ratio.

with the gallium content and also leading to a reduced energy splitting of the p-type orbitals. Figures 8(c) and 8(d) show a monotonic blue- and red-shift for an increasing QD height for a constant base diameter, i.e., an increasing aspect ratio and a decreasing aspect ratio at constant height, respectively. An energetic red-shift can be achieved by increasing QD size at constant aspect ratio [Fig. 8(e)], with the red symbols showing $In_{0.5}Ga_{0.5}As$ QDs, shifting the transitions further to lower energies and decreasing the splitting of the p-type orbitals, cf. Fig. 8(b). We discuss the global minimum in Figs. 8(a) and 4(a) by considering the impact of barrier width and hydrostatic strain on the energy of the intraband transitions. Figures 9(a) and 9(b) depict the energies of the p-to-s transitions as a function of barrier width for a stack of two QDs, wherein Fig. 9(a) strain, as well as piezoelectric fields, are neglected and in Fig. 9(b) strain is included but piezoelectricity is omitted. With neglected strain and piezoelectricity, the transition energies show a monotonous decrease with increasing barrier width (red-shift). This is linked to the increasing volume of the orbitals, cf. black diamonds in Fig. 9(a) since, with increasing separation of the QDs, a growing part of the electron densities is located in-between the QDs. The density's volume

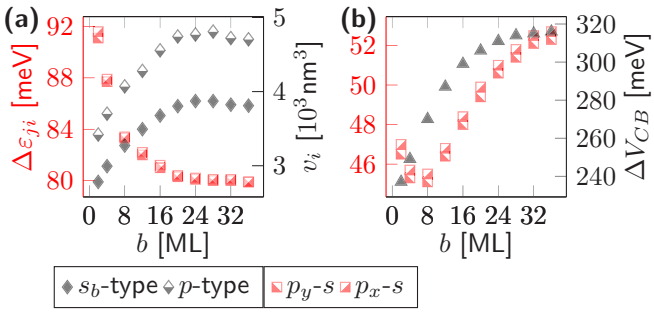

FIG. 9. Evolution of the energies $\Delta\varepsilon_{ji}$ of the p-to-s intraband transitions in a stack of two identical QDs as a function of barrier width b (red semifilled squares). (a) The transition energies omitting strain as well as piezoelectricity and the volume v_i of the corresponding binding s-type and the p-type orbitals (black filled and semifilled diamonds). v_i is the volume of the orbital i at which the electron density is $\geqslant 0.1\%$ of its maximum value. (b) The transition energies including strain but neglecting piezoelectricity. V_{CB} depicts the depth of the QDs potential well measured in the mid of the top QD, i.e., the minimum of the conduction band edge. The transition energies were calculated using the 8-band $\boldsymbol{k}\cdot\boldsymbol{p}$ model.

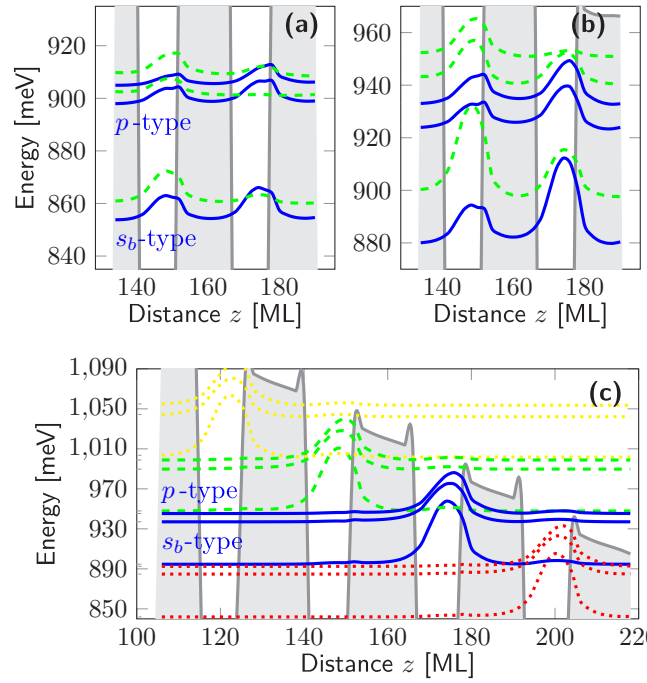

FIG. 10. The V_{CB} band-structure staircase potential for the two central QDs in a stack of ten identical $In_{1.0}Ga_{0.0}As/GaAs$ QDs separated by $b = 16$ MLs at various external biases E_{ext}. Gray lines and shaded areas depict the calculated conduction band-edge and barrier material, respectively. Colored lines show the $|\psi_i(z)|^2$ of the s- and p-type Kramers-degenerate electron states for the QDs in the central region, showing a maximum probability density. (a) The staircase potential without an external bias. (b) The staircase potential at $E_{\mathrm{ext}} = 24$ kVcm^{-1}. Solid blue and dashed green lines depict the s_b- and p-type orbitals discussed in Sec. III C. (c) the staircase potential at $E_{\mathrm{ext}} = 72$ kVcm^{-1} showing four central QDs.

decreases again for $b \geqslant 32$ MLs, as the QDs decouple and the electrons more localized. The inclusion of strain into the transition energies calculation already shows the global minimum, cf. Fig. 9(b). With increasing barrier width, the depth of the QDs potential well ΔV_{CB}, cf. black triangles in Fig. 9(b), is increasing as the hydrostatic strain decreases, cf. Fig. 7(b), resulting in a blue-shift of the transition energies. This effect dominates for barrier widths of $b \gtrsim 8$ MLs, whereas in the strong coupling regime, the red-shift resulting from an increasing volume of the electron orbitals is prevailing.

D. Intraband staircase potential design

In this section, we show that an intraband staircase potential of subsequent, identical intraband transitions can be realized in such stacks of QDs. In Fig. 10, the conduction band staircase potential for the two central QDs in a stack of ten QDs at various external biases are shown, illustrating its influence on the state's energy and delocalization. The colored lines show the probability densities of the Kramers-degenerate electron states exhibiting a maximum within the two central QDs, whose p-to-s transition energies correspond to the discussion in the previous Sec. III C and Fig. 8. Figures 10(a) and 10(b) show the V_{CB} band structure without and with an external bias of $E_{\mathrm{ext}} = 24$ kVcm^{-1}, respectively, which has basically three effects on the staircase potential: With increasing external bias, the energetic distances of the s- and p-type orbitals between the adjacent QDs, i.e., interdot s-to-s or p-to-p transition, depicted by the solid blue and dashed green lines, respectively, are increasing. In contrast, the energies of the p-to-s intradot transitions remain almost constant; see Fig. 11 for an evolution of the intradot transition energies as a function of the external bias. A third effect is the increasing localization of the states with the bias. Figure 10(c) shows the staircase potential at an external bias of $E_{\mathrm{ext}} = 72$ kVcm^{-1}, where the probability densities of the s- and p-type orbitals are almost completely located in their respective QDs.

Lastly, we examine the electronic structure of an exemplary stack of 20 coupled QDs under external bias and show that transition energies can be engineered to provide optical gain in the infrared spectral range. Figure 12 shows a zoom into the relevant conduction band region for a stack of 20 identical $In_{0.8}Ga_{0.2}As/GaAs$ QDs with a height of 5 MLs and a diameter of 36 MLs as discussed in Sec. III, separated by $b = 8$ MLs, at an external bias of $E_{\mathrm{ext}} = 32$ kVcm^{-1}. For the

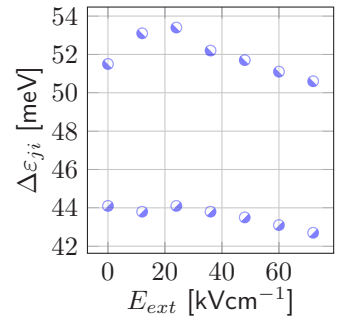

FIG. 11. Evolution of the energy $\Delta\varepsilon_{ji}$ of the p-to-s intraband transitions for the two central QDs in a stack of ten $In_{1.0}Ga_{0.0}As/GaAs$ QDs separated by barriers of $b = 16$ MLs as a function of external bias E_{ext}.

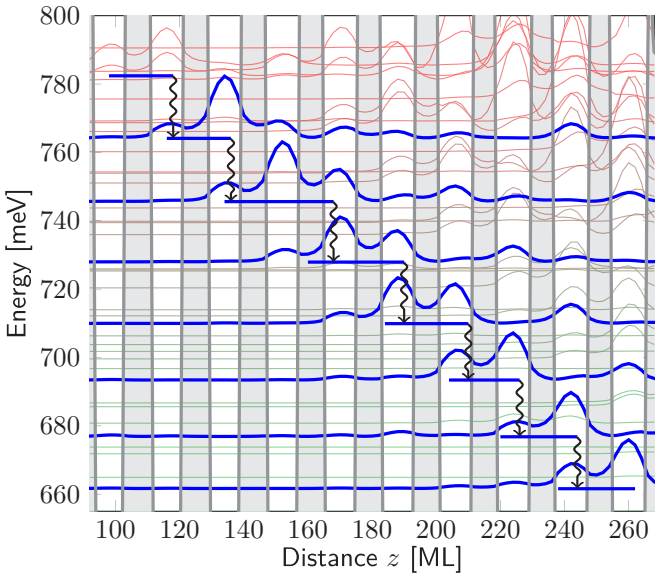

FIG. 12. The V_{CB} band-structure staircase potential for a stack of 20 identical $In_{0.8}Ga_{0.2}As/GaAs$ QDs with basis lengths and heights of 14.7 nm and 2.8 nm, respectively, at an external bias of $E_{\mathrm{ext}} = 32\,\mathrm{kVcm}^{-1}$. The barrier width is set to 8 MLs. Wavy arrows indicate possible intraband transitions. A plot of the full band-structure staircase potential is provided in the Supplemental Material [22].

chosen number of QDs, at least seven transitions at an energy of ≈17.2 meV are present in the stack's central part. After edge effects are converged, suitable transitions scale with the QD-chain length, i.e., the gain. Carriers subsequently occupy the ground state within a QD and an excited state of the adjacent QD, building pairwise electronically coupled QDs along the chain. The orbitals show an *s*-type symmetry within a QD. These transitions within coupled QDs, like the *p*-to-*s* transitions in Fig. 8, can be tuned using barrier width, material composition, and external bias allowing, for example, an effective relaxation via LO phonons. To achieve population inversion, however, an additional *p*-to-*s* or *s*-to-*p* transition within the staircase potential is required. Due to the comparatively low intradot transition energies close to the materials LO-phonon energy, cf. Fig. 8, this transition could be achieved rather than a diagonal transition across an additional barrier. A suitable QCL band-structure design based on coupled two-QD unit cells, enabling population inversion as well as providing a wavelength within the far-infrared, is developed and discussed in the associated paper Ref. [17].

IV. CONCLUSION

We developed a novel method for calculating excited states in electronically coupled QD systems based on QD single-particle wave functions, enabling and accelerating the calculation of the band structure of QD stacks consisting of 20 and more QDs, including dozens of electronic states at a affordable computational cost. Facilitated by the LCQO method, we investigated the evolution of conduction band states as a function of various QD parameters, which is a prerequisite for developing suitable active regions of QD-QCLs. With this, we demonstrated an exemplary staircase potential with equally distributed energy transitions and probability densities at an external bias. Our methodology paves the way for developing an active region of a QCL based on a QD superlattice, exploiting the intrinsic advantages of QDs, which can lead to low threshold current densities and elevated operating temperatures, with particular significance in the far-infrared spectral range.

ACKNOWLEDGMENT

The Deutsche Forschungsgemeinschaft partly funded this work in the framework of the SFB 787 (Grant No. 43659573).

[1] R. A. Suris, Prospects for quantum dot structures applications in electronics and optoelectronics, in *Future Trends in Microelectronics*, edited by S. Luryi, J. Xu, and A. Zaslavsky (Springer, Dordrecht, The Netherlands, 1996), pp. 197–208.

[2] I. A. Dmitriev and R. A. Suris, Quantum cascade lasers based on quantum dot superlattice, Phys. Status Solidi A **202**, 987 (2005).

[3] N. Wingreen and C. Stafford, Quantum-dot cascade laser: proposal for an ultralow-threshold semiconductor laser, IEEE J. Quantum Electron. **33**, 1170 (1997).

[4] C.-F. Hsu, J.-S. O, P. Zory, and D. Botez, Intersubband quantum-box semiconductor lasers, IEEE J. Sel. Top. Quantum Electron. **6**, 491 (2000).

[5] V. M. Apalkov and T. Chakraborty, Influence of dimensionality on the emission spectra of nanostructures, Appl. Phys. Lett. **83**, 3671 (2003).

[6] N. Vukmirovic, D. Indjin, Z. Ikonic, and P. Harrison, Electron Transport and Terahertz Gain in Quantum-Dot Cascades, IEEE Photon. Technol. Lett. **20**, 129 (2008).

[7] N. Zhuo, F. Liu, J. Zhang, L. Wang, J. Liu, S. Zhai, and Z. Wang, Quantum dot cascade laser, Nanoscale Res. Lett. **9**, 144 (2014).

[8] J. Alton, S. Barbieri, J. Fowler, H. E. Beere, J. Muscat, E. H. Linfield, D. A. Ritchie, G. Davis, R. Köhler, and A. Tredicucci, Magnetic field in-plane quantization and tuning of population inversion in a THz superlattice quantum cascade laser, Phys. Rev. B **68**, 081303(R) (2003).

[9] V. Tamosiunas, R. Zobl, J. Ulrich, K. Unterrainer, R. Colombelli, C. Gmachl, K. West, L. Pfeiffer, and F. Capasso, Terahertz quantum cascade lasers in a magnetic field, Appl. Phys. Lett. **83**, 3873 (2003).

[10] G. Scalari, S. Blaser, J. Faist, H. Beere, E. Linfield, D. Ritchie, and G. Davies, Terahertz Emission from Quantum Cascade Lasers in the Quantum Hall Regime: Evidence for Many Body Resonances and Localization Effects, Phys. Rev. Lett. **93**, 237403 (2004).

[11] F. Valmorra, G. Scalari, K. Ohtani, M. Beck, and J. Faist, InGaAs/AlInGaAs THz quantum cascade lasers operating up to 195 K in strong magnetic field, New J. Phys. **17**, 023050 (2015).

[12] M. Korkusiński and P. Hawrylak, Electronic structure of vertically stacked self-assembled quantum disks, Phys. Rev. B **63**, 195311 (2001).

[13] W. Jaskólski, M. Zieliński, G. W. Bryant, and J. Aizpurua, Strain effects on the electronic structure of strongly coupled self-assembled InAs/GaAs quantum dots: Tight-binding approach, Phys. Rev. B **74**, 195339 (2006).

[14] M. Usman, S. Ahmed, and G. Klimeck, A tight binding study of strain-reduced confinement potentials in identical and non-identical InAs/GaAs vertically stacked quantum dots, in *2008 8th IEEE Conference on Nanotechnology* (IEEE, Arlington, Texas, 2008), pp. 541–544.

[15] M. Usman, T. Inoue, Y. Harda, G. Klimeck, and T. Kita, Experimental and atomistic theoretical study of degree of polarization from multilayer InAs/GaAs quantum dot stacks, Phys. Rev. B **84**, 115321 (2011).

[16] T. Saito, H. Ebe, Y. Arakawa, T. Kakitsuka, and M. Sugawara, Optical polarization in columnar InAs/GaAs quantum dots: 8-band k·p calculations, Phys. Rev. B **77**, 195318 (2008).

[17] A. Mittelstädt, L. A. Th. Greif, S. T. Jagsch, and A. Schliwa, Terahertz lasing at room temperature: A numerical study of a vertical-emitting quantum cascade laser based on a quantum dot superlattice, Phys. Rev. B **103**, 115301 (2021).

[18] R. A. Ėvarestov, *Quantum Chemistry of Solids: The LCAO First Principles Treatment of Crystals*, Springer Series in Solid-State Sciences Vol. 153 (Springer, Berlin, 2007).

[19] M. Grundmann, O. Stier, and D. Bimberg, InAs/GaAs pyramidal quantum dots: Strain distribution, optical phonons, and electronic structure, Phys. Rev. B **52**, 11969 (1995).

[20] O. Stier, M. Grundmann, and D. Bimberg, Electronic and optical properties of strained quantum dots modeled by 8-band k·p theory, Phys. Rev. B **59**, 5688 (1999).

[21] A. Schliwa, M. Winkelnkemper, and D. Bimberg, Impact of size, shape, and composition on piezoelectric effects and electronic properties of In(Ga)As/GaAs quantum dots, Phys. Rev. B **76**, 205324 (2007).

[22] See Supplemental Material at http://link.aps.org/supplemental/10.1103/PhysRevB.103.115302 for a convergence analysis, the full band structure staircase potential, and the features of the $\boldsymbol{k \cdot p}$ method.

[23] M. Wagner, *Gruppentheoretische Methoden in der Physik: ein Lehr-und Nachschlagewerk*, Vieweg-Lehrbuch Mathematische Physik (Vieweg, Braunschweig, 1998).

[24] G. Bester, X. Wu, D. Vanderbilt, and A. Zunger, Importance of Second-Order Piezoelectric Effects in Zinc-Blende Semiconductors, Phys. Rev. Lett. **96**, 187602 (2006).

[25] G. Bester, A. Zunger, X. Wu, and D. Vanderbilt, Effects of linear and nonlinear piezoelectricity on the electronic properties of InAs/GaAs quantum dots, Phys. Rev. B **74**, 081305(R) (2006).

[26] L. C. Lew Yan Voon and M. Willatzen, *The k-p Method: Electronic Properties of Semiconductors* (Springer, Dordrecht, The Netherlands, 2009).

[27] E. O. Kane, in *Handbook on Semiconductors*, edited by W. Paul (North-Holland, Amsterdam, 1982), Vol. 1.

[28] O. Stier and D. Bimberg, Modeling of strained quantum wires using eight-band **k·p** theory, Phys. Rev. B **55**, 7726 (1997).

[29] O. Stier, *Electronic and Optical Properties of Quantum Dots and Wires* (Wissenschaft & Technik Verlag, Berlin, 2000).

[30] G. Bastard, Superlattice band structure in the envelope-function approximation, Phys. Rev. B **24**, 5693 (1981).

[31] *Properties of Lattice-Matched and Strained Indium Gallium Arsenide*, edited by P. Bhattacharya (INSPEC, Institution of Electrical Engineers, London, 1993).

[32] *Landolt-Börnstein: Numerical Data and Functional Relationships in Science and Technology–New Series*, edited by O. Madelung, H. Landolt, R. Börnstein, and W. Martienssen, (Springer, Berlin, 1982).

[33] S. Adachi, *Physical Properties of III-V Semiconductor Compounds: InP, InAs, GaAs, GaP, InGaAs, and InGaAsP* (Wiley, New York, 1992).

[34] D. Gershoni, C. Henry, and G. Baraff, Calculating the optical properties of multidimensional heterostructures: Application to the modeling of quaternary quantum well lasers, IEEE J. Quantum Electron. **29**, 2433 (1993).

[35] I. Vurgaftman, J. R. Meyer, and L. R. Ram-Mohan, Band parameters for III-V compound semiconductors and their alloys, J. Appl. Phys. **89**, 5815 (2001).

[36] S. L. Chuang, *Physics of Optoelectronic Devices*, 2nd ed., Wiley Series in Pure and Applied Optics (John Wiley & Sons, Hoboken, NJ, 2009).

[37] T. E. Ostromek, Evaluation of matrix elements of the $8\times8\,\mathbf{k}\cdot\mathbf{p}$ Hamiltonian with **k** -dependent spin-orbit contributions for the zinc-blende structure of GaAs, Phys. Rev. B **54**, 14467 (1996).

[38] H. Blank, D. Litvinov, R. Schneider, D. Gerthsen, T. Passow, and K. Scheerschmidt, Quantification of the In-distribution in embedded InGaAs quantum dots by transmission electron microscopy, Cryst. Res. Technol. **44**, 1083 (2009).

[39] D. Litvinov, H. Blank, R. Schneider, D. Gerthsen, T. Vallaitis, J. Leuthold, T. Passow, A. Grau, H. Kalt, C. Klingshirn, and M. Hetterich, Influence of InGaAs cap layers with different In concentration on the properties of InGaAs quantum dots, J. Appl. Phys. **103**, 083532 (2008).

[40] S. Yamauchi, K. Komori, I. Morohashi, K. Goshima, and T. Sugaya, Electronic structures in single pair of InAs/GaAs coupled quantum dots with various interdot spacings, J. Appl. Phys. **99**, 033522 (2006).

[41] D. M. Bruls, P. M. Koenraad, H. W. M. Salemink, J. H. Wolter, M. Hopkinson, and M. S. Skolnick, Stacked low-growth-rate InAs quantum dots studied at the atomic level by cross-sectional scanning tunneling microscopy, Appl. Phys. Lett. **82**, 3758 (2003).

[42] T. Sugaya, Y. Kamikawa, S. Furue, T. Amano, M. Mori, and S. Niki, Multi-stacked quantum dot solar cells fabricated by intermittent deposition of InGaAs, Sol. Energy Mater. Sol. Cells **95**, 163 (2011).

[43] A. Lemaître, G. Patriarche, and F. Glas, Composition profiling of InAs/GaAs quantum dots, Appl. Phys. Lett. **85**, 3717 (2004).